

Microscopic structure of three-dimensional charge order in kagome superconductor AV_3Sb_5 and its tunability

Mingu Kang^{1,2*†}, Shiang Fang^{1*}, Jonggyu Yoo^{2,3*}, Brenden R. Ortiz⁴, Yuzki Oey⁴, Sae Hee Ryu⁵, Jimin Kim⁶, Chris Jozwiak⁵, Aaron Bostwick⁵, Eli Rotenberg⁵, Efthimios Kaxiras^{7,8}, Joe Checkelsky¹, Stephen D. Wilson⁴, Jae-Hoon Park^{2,3†} & Riccardo Comin^{1†}

¹Department of Physics, Massachusetts Institute of Technology, Cambridge, Massachusetts 02139, USA.

²Max Planck POSTECH Korea Research Initiative, Center for Complex Phase of Materials, Pohang 790-784, Republic of Korea.

³Department of Physics, Pohang University of Science and Technology, Pohang 790-784, Republic of Korea.

⁴Materials Department and California Nanosystems Institute, University of California Santa Barbara, Santa Barbara, California 93106, USA.

⁵Advanced Light Source, E. O. Lawrence Berkeley National Laboratory, Berkeley, California 94720, USA.

⁶Center for Artificial Low Dimensional Electronic Systems, Institute for Basic Science (IBS), Pohang 790-784, Republic of Korea.

⁷Department of Physics, Harvard University, Cambridge, Massachusetts 02139, USA.

⁸John A. Paulson School of Engineering and Applied Sciences, Harvard University, Cambridge, Massachusetts 02138, USA.

*These authors contributed equally to this work.

†Correspondence should be addressed to iordia@mit.edu, jhp@postech.ac.kr, rcomin@mit.edu.

Correlated electronic systems are naturally susceptible to develop collective, symmetry-breaking electronic phases as observed in Cu- and Fe-based high-temperature superconductors, and twisted Moiré superlattices. The family of kagome metals AV_3Sb_5 ($A = K, Rb, Cs$) is a recently discovered, rich platform to study many of these phenomena and their interplay. In these systems, three-dimensional charge order (3D-CO) is the primary instability that sets the stage in which other ordered phases emerge, including unidirectional stripe order, orbital flux order, and superconductivity. Therefore, determining the exact nature of the 3D-CO is key to capture the broader phenomenology in AV_3Sb_5 . Here, we use high-resolution angle-resolved photoemission spectroscopy to resolve the microscopic structure and symmetry of 3D-CO in AV_3Sb_5 . Our approach is based on identifying an unusual splitting of kagome bands induced by 3D-CO, which provides a sensitive way to refine the spatial charge patterns in neighboring kagome planes. Notably, we found a marked dependence of the 3D-CO structure on alkali metal and doping: the 3D-CO in CsV_3Sb_5 is composed of kagome layers with alternating Star-of-David and Tri-Hexagonal distortions, while KV_3Sb_5 , RbV_3Sb_5 , and Sn-doped CsV_3Sb_5 realize a staggered charge pattern breaking C_6 rotational symmetry. These results establish the microscopic structure of 3D-CO and its evolution with chemical composition for the first time, providing fresh insights on the origin of the cascade of exotic electronic phases in AV_3Sb_5 .

The family of AV_3Sb_5 is a newly discovered series of kagome-based compounds realizing unconventional many-body phases and nontrivial electronic topology (Fig. 1c,d)^{1,2}. In close analogy with other strongly correlated systems such as Cu-³ and Fe-based high-temperature superconductors⁴, as well as twisted Moiré superlattices⁵, a cascade of coupled symmetry-broken electronic orders has been observed in AV_3Sb_5 . These include translational symmetry breaking in the form of 2×2 charge order (CO) below $T_{CO} \approx 78\sim 102$ K^{2,6}, rotational symmetry breaking in the form of unidirectional 1×4 stripe order below $T_{SO} \approx 50\sim 60$ K⁷⁻¹⁰, a time-reversal symmetry breaking orbital flux phase below $T_f \approx 70$ K¹¹, and superconductivity below $T_c \approx 0.92\sim 2.5$ K^{2,12,13}. Understanding the origin, nature, and interrelation between these electronic orders is a major frontier of this emerging research field.

Notably, previous theoretical and experimental investigations point toward the unique role of the electronic structure of the underlying kagome lattice in driving the rich physics of AV_3Sb_5 ¹⁴⁻²⁰. In the ideal limit, the kagome lattice exhibits multiple singularities in its electronic dispersion, including Dirac fermions at the Brillouin zone corner K , van Hove singularity (vHS) at the zone edge M , and flat bands across the whole Brillouin zone (Fig. 1a). Depending on the band filling fraction n , these electronic states may engender various topological and correlated phases as extensively investigated for more than a decade²¹⁻²⁶. Especially at the vHS filling fractions $n = 3/12$ and $5/12$ (Fig. 1a), the Fermi surface of the kagome lattice is perfectly nested by three symmetry-equivalent reciprocal lattice vectors $Q_1 = (0.5, 0)$, Q_2 , and Q_3 (Fig. 1b). Combined with the high density of states at vHS, the nesting creates a diverging electronic susceptibility and sets the stage for pairing in multiple channels, and the subsequent emergence of charge/spin order and superconductivity²⁴⁻²⁶. The electronic structure of the AV_3Sb_5 series follows this script, with multiple kagome-derived vHS sharply aligned to the Fermi level (E_F)¹⁶⁻²⁰. Accordingly, as displayed in Fig. 1e, density functional theory (DFT) calculation of phonon frequency reveals six unstable modes exactly at the Q_1 , Q_2 , and Q_3 in-plane wave vectors – three at M ($k_z = 0$) and the other three at L ($k_z = \pi$) – indicating that the pristine kagome structure is unstable toward the 2×2 charge distortion²⁷⁻²⁹. Combined with the experimental identification of the 2×2 CO^{2,6}, this suggests that the toy-model vHS physics of the ideal kagome lattice is indeed realized within AV_3Sb_5 system.

Importantly, the contribution of L phonons with nonzero out-of-plane momentum ($k_z = \pi$) indicates that the full description of CO in the AV_3Sb_5 series needs to go beyond the limit of two-

dimensional kagome lattice. The three-dimensional nature of CO was reported in early studies^{17,30}, supporting either twofold ($2\times 2\times 2$) or fourfold ($2\times 2\times 4$) c -axis modulations^{31,32}. As we illustrate in Fig. 1f,g, M -point (L -point) phonons are associated to V-V bond distortions in-phase (out-of-phase) across neighboring kagome planes (Fig. 1f)²⁸. Then, depending on the possible $3Q$ combinations of M and L phonons, various microscopic 3D-CO structures can be realized in the AV_3Sb_5 series (Fig. 1h-m): Star-of-David or SoD ($-M, -M, -M$); Tri-hexagonal or TrH (M, M, M); Alternating SoD and TrH (L, L, L); Staggered SoD ($-M, -L, -L$); Staggered TrH (M, L, L); and Staggered Alternating SoD and TrH (M, M, L).

We emphasize here that identifying the exact structure and symmetry of 3D-CO is of paramount importance for understanding the sequence of electronic symmetry breaking transitions observed in AV_3Sb_5 . This is because CO formation has the highest energy scale in AV_3Sb_5 series ($T_{CO} \approx 78\sim 102$ K) and thus defines the background symmetry under which other electronic phases emerge (stripe order, nematicity, flux phase, and superconductivity). As an example, if CO crystallizes in the inverse MLL , MLL , or MML phases (Fig. 1k-m), C_6 -rotational symmetry is spontaneously broken, which may provide a natural explanation for the unidirectional 1×4 stripe order and electronic nematicity emerging below T_{CO} ⁷⁻¹⁰. However, the detailed microscopic structure of 3D-CO and its composition dependence in AV_3Sb_5 series have not been conclusively reported so far, with different approaches – X-ray diffraction^{31,32}, coherent phonon spectroscopy³³, nuclear magnetic/quadrupole resonance³⁴, scanning tunneling microscopy²⁷, and DFT³⁵ – yielding divergent results.

In the present study, we establish the microscopic structure of 3D-CO and its evolution in the AV_3Sb_5 series by analyzing the detailed reconstruction of the electronic bands induced by 3D-CO. Using high-resolution angle-resolved photoemission spectroscopy (ARPES), we observe an unusual energy splitting of the kagome-derived vHS and Dirac bands, which is a direct consequence of the unit cell reconstruction in the 3D-CO phase. Crucially, the precise morphology of the band splitting is highly sensitive to the intra-unit-cell stacking between different 3D-CO modulation patterns across adjacent kagome planes, which allows us to constrain the 3D-CO structure and symmetry in the AV_3Sb_5 series. Using this approach, we determine that the band splitting of CsV_3Sb_5 is most consistent with the Alternating SoD and TrH structure (LLL phase), while those in KV_3Sb_5 , RbV_3Sb_5 , and Sn-doped CsV_3Sb_5 are markedly different from the CsV_3Sb_5 and can be assigned to the inverse MLL or MML phases. These results expand our current

understanding of CO in the AV_3Sb_5 series, and reveal new essential details to explain the origin of multiple collective phenomena realized in strongly correlated kagome systems.

We start with a brief description of the overall electronic structure of AV_3Sb_5 . As displayed in Fig. 2a, the DFT band calculation for CsV_3Sb_5 reveals four bands near E_F : an electron-pocket at the Brillouin zone center Γ (G -band), $d_{xy}/d_{x^2-y^2}$ orbital kagome bands with Dirac point at ≈ -0.27 eV and vHS near E_F ($K1$ -band), d_{xz}/d_{yz} orbital kagome bands with Dirac point at ≈ -1.08 eV and vHS near E_F ($K2$ -band), and additional d_{xz}/d_{yz} orbital kagome bands with opposite parity from the $K2$ -band ($K2'$ -band). All band dispersions have been closely reproduced in previous ARPES studies^{19,20,36-38}. Meanwhile, we note that in the experimental geometry used in the present study, only G -, $K1$ -, and $K2$ -bands are visible in the ARPES spectra (see Fig. 2c for example) due to the destructive interference of photoelectrons from the $K2'$ -band³⁹.

As summarized in Fig. 2, we observed two distinct electronic reconstructions induced by 3D-CO in CsV_3Sb_5 . First, as shown in Fig. 2b-d, we detected clear shadow bands below T_{CO} (dashed arrows in Fig. 2d), which are the replica of the original bands (solid arrows in Fig. 2c,d) folded along the in-plane momentum direction. This is a direct consequence of the new periodicity arising from the in-plane component of charge order, which folds the pristine Brillouin zone to the smaller 2×2 CO Brillouin zone (see schematics in Fig. 2b). Such shadow bands and in-plane folding effects have been typically observed in other charge order systems such as transition metal dichalcogenides⁴⁰ and rare-earth trichalcogenides⁴¹. At the same time, as shown in Fig. 2e-k, a detailed inspection below T_{CO} additionally reveals an unusual doubling or splitting of the kagome bands along the energy axis. Such splitting, which is unreported, could be visualized only after careful optimization of the spectral quality (see also Fig. 4f for corresponding energy and momentum distribution curves). At the simplest level, one can understand the band doubling as a consequence of the out-of-plane component of the 3D-CO, which folds the Brillouin zone along the k_z -direction and superimposes the $k_z = \pi \sim \pi/2$ bands onto the $k_z = 0 \sim \pi/2$ bands (see schematics in Fig. 2e). In the case of CsV_3Sb_5 , we find three sectors in the band structure where the doubling becomes most prominent: near the vHS of the $K1$ -band (Fig. 2g,j), at the lower Dirac band of the $K1$ -band (Fig. 2g,i), and at the $K2$ -band near E_F (Fig. 2k).

The key idea of our study comes from the recognition that the doubled-band dispersion in the 3D-CO state is actually more than the simple superposition of $k_z = 0 \sim \pi/2$ and $k_z = \pi \sim \pi/2$ bands of the pristine structure. In the 3D-CO state, the adjacent kagome layers in AV_3Sb_5 become distinct

upon realizing different CO patterns on each layer (Fig. 1j-m). The altered hopping pathways between the two charge-ordered kagome planes further modifies the doubled-band dispersion. This mechanism depends on the detailed lattice reconstructions in adjacent kagome planes, with the nature of the band splitting becoming strongly dependent on the 3D-CO structure. This provides a unique and highly constrained way to resolve the microscopic structure of 3D-CO in AV_3Sb_5 series.

To illustrate this idea further, we simulated the reconstruction of CsV_3Sb_5 bands in all possible 3D-CO structures using DFT. Fig. 3a-f represents the electronic structure of CsV_3Sb_5 at $k_z = 0$ in the inverse MMM , MMM , LLL , inverse MLL , MLL , and MML phases, respectively. Note that, for simplicity, we unfolded the band structure along the in-plane momentum-space, while keeping the band folding along k_z . In accordance with the experimental results, the doubling of the dispersions for the $K1$ - and $K2$ -kagome bands are closely reproduced in the 3D-CO states (see yellow arrows in Fig. 3c for example). Most importantly, the details of band splitting are highly dependent on the microscopic structure of 3D-CO. The most noticeable discriminant between different 3D-CO structures is the behavior of the lower $K1$ -Dirac band. As marked with yellow arrows in the insets of Fig. 3, the lower $K1$ -Dirac band barely splits in the inverse MMM , MMM , inverse MLL , and MLL structures (Fig. 3a,b,d,e), while an apparent doubling is observed in the LLL structure (Fig. 3c). This is closely reproduced by the ARPES spectra of Fig. 2g,i. For the case of the MML structure (Fig. 3f), both the lower $K1$ -Dirac band and $K1$ -vHS band split into at least three bands if one takes an average over all possible C_2 -symmetric domains. Based on the above considerations, we conclude that the observed band splitting supports the LLL structure or Alternating SoD and TrH phase (Fig. 1j) as the microscopic 3D-CO structure in CsV_3Sb_5 .

Intriguingly, the investigation of KV_3Sb_5 , RbV_3Sb_5 , and Sn-doped CsV_3Sb_5 revealed an electronic reconstruction markedly different from the CsV_3Sb_5 case. Figure 4 displays ARPES spectra of KV_3Sb_5 , RbV_3Sb_5 , and Sn-doped CsV_3Sb_5 measured at 6 K, in the CO state. Similar to the case of CsV_3Sb_5 , the doubling or splitting of the $K1$ -vHS (Fig. 4a,b,c) and $K2$ -bands (Fig. 4d,e) is clearly observed across the whole family. The corresponding energy distribution curves of the $K1$ -vHS and momentum-distribution curves of the $K2$ -band (Fig. 4f,g) also unambiguously demonstrate the presence of band doubling. These results indicate that the 3D-CO is a universal phenomenon in the AV_3Sb_5 series. However, we observe that the behavior of lower $K1$ Dirac band in KV_3Sb_5 , RbV_3Sb_5 , and Sn-doped CsV_3Sb_5 is very different from that of the CsV_3Sb_5 case. As highlighted with yellow arrows in Fig. 4a-e, the lower Dirac dispersion of the $K1$ band does not

undergo a splitting in the 3D-CO state, in contrast to the observations in CsV_3Sb_5 (Fig. 2g,i). Compared to the calculations in Fig. 3, this behavior rules out the *LLL* and *MML* structures (Fig. 3c,f) but is consistent with the inverse *MMM*, *MMM*, inverse *MLL*, and *MLL* structures (Fig. 3a,b,d,e). In case of the inverse *MMM* and *MMM* structures however, the charge distortions do not distinguish the neighboring kagome planes (i.e. $2\times 2\times 1$ structure) and cannot induce the out-of-plane band doubling observed on K1-vHS and K2-band. We thus conclude that the 3D-CO in KV_3Sb_5 , RbV_3Sb_5 , and Sn-doped CsV_3Sb_5 manifests in the inverse *MLL* or *MLL* phases (intrinsically breaking C_6 -rotational symmetry) at variance with the *LLL* structure in pristine CsV_3Sb_5 . This implies that despite the charge ordering tendency of the kagome lattice is universal in $AV_3\text{Sb}_5$ family, the microscopic details of 3D-CO are strongly dependent on the chemical composition and doping, adding to the rich physics that can be realized in the $AV_3\text{Sb}_5$ series.

Lastly, we discuss the insights obtained from our results in relation to the existing literature. Previous DFT calculations have revealed that the net energy of $AV_3\text{Sb}_5$ only marginally depends on the out-of-plane structure of 3D-CO, indicating that the charge order is only weakly correlated along the c -axis³⁵. It is thus quite possible that the detailed microscopic structure of 3D-CO varies sensitively depending on the interlayer spacing or strength of the inter-kagome-layer interactions, which can be controlled by the alkali metal element¹ or Sn-doping to Sb1 sites⁴². Intriguingly, several DFT studies have predicted the *MLL* structure or Staggered TrH phase to be the ground state of $AV_3\text{Sb}_5$ ^{29,33}, consistent with our conclusions for KV_3Sb_5 , RbV_3Sb_5 , and Sn-doped CsV_3Sb_5 . In the case of pristine CsV_3Sb_5 , it is still being debated whether the 3D-CO manifests in the $2\times 2\times 2$ form as in the K and Rb counterparts, or in a more complicated $2\times 2\times 4$ pattern^{31,32}. Nevertheless, the X-ray structural refinements on CsV_3Sb_5 revealed the modulation pattern containing an alternating TrH and SoD structure without staggering³¹, in close analogy with the *LLL* structure obtained here. We note that in CsV_3Sb_5 , signatures of bulk rotational symmetry breaking and surface stripe order emerge only below the characteristic temperature $T_{\text{SO}} \approx 60$ K and not in the pure charge-ordered state between $T_{\text{CO}} \approx 94$ K and $T_{\text{SO}} \approx 60$ K^{7,10}. This suggests that the 3D-CO itself does not break C_6 rotational symmetry, which is indeed the case for the *LLL* structure revealed in the present study (Fig. 1j). The nematicity and surface stripe order observed in CsV_3Sb_5 thus represent additional emergent electronic symmetry breaking that are independent of the 3D-CO. In contrast, we conclude that the C_6 rotational symmetry to be already broken in the 3D-CO phase of $(\text{K,Rb})\text{V}_3\text{Sb}_5$ with the *MLL* or inverse *MLL* structure (Fig. 1k,l). Indeed, the Fourier-

transformed scanning tunneling spectroscopy on KV_3Sb_5 revealed that the symmetry of system is reduced to C_2 in the charge-ordered state even without stripe ordering⁹. However, the phenomena of 3D-CO and rotational symmetry breaking are much less explored in $(K,Rb)V_3Sb_5$ compared to the Cs case – the present results thus invite future X-ray diffraction, nuclear magnetic resonances, and transport investigations on the full series.

In conclusion, we establish the microscopic structure of 3D-CO and its tunability in the family of topological kagome metals $AV_3(Sb,Sn)_5$. Determining the exact structure of 3D-CO is a topic of great relevance, as it sets the background symmetry of the system under which other many-body effects emerge. Combining high-resolution ARPES and DFT supercell calculations, we resolve the detailed electronic reconstruction of the kagome bands in the 3D-CO state. We reveal that the 3D-CO in CsV_3Sb_5 consists of a stacking of kagome layers with alternating SoD and TrH distortions (*LLL*), while KV_3Sb_5 , RbV_3Sb_5 , and Sn-doped CsV_3Sb_5 realize the staggered CO structure breaking the C_6 rotational symmetry (*MLL* or inverse *MLL*). The remarkable tunability of the 3D-CO state across otherwise similar compounds suggests that the AV_3Sb_5 series is a candidate host for an extremely rich phase diagram of emergent electronic phases, enabling new opportunities for fundamental studies at the nexus of strong correlation phenomena and topology.

Methods

Sample synthesis and angle-resolved photoemission spectroscopy

High-quality single crystals of pristine and Sn-doped AV_3Sb_5 were synthesized via flux method as described in Ref.^{1,2,42}. ARPES experiments were performed at Beamline 7.0.2 (MAESTRO) of the Advanced Light Source, equipped with R4000 hemispherical electron analyzer (Scienta Omicron). The samples were cleaved inside an ultrahigh vacuum chamber with a base pressure better than $\approx 4 \times 10^{-11}$ torr. We keep the following experimental geometry throughout the measurement: horizontal analyzer slit, linear horizontal light polarization, and Γ -K-M direction of the sample aligned to the scattering plane. For each sample, photon energy was scanned from 60 eV to 200 eV, covering more than three complete three-dimensional Brillouin zone. For the high-resolution data in Fig. 2,4, we selected the photon energies for each sample that best visualize the band splitting. The energy and momentum resolutions were better than 20 meV and 0.01 \AA^{-1} .

Density functional theory calculations

DFT calculations were performed using the Vienna Ab initio Simulation Package^{43,44}, with GGA-PBE exchange-correlation functional⁴⁵ and the pseudo potential formalism based on the Projector Augmented Wave method⁴⁶. The phonon frequency spectrum was derived from the Hessian matrix (which encodes the second derivatives of the atomic position coordinate) computed with the density-functional-perturbation theory (DFPT) method, using a $4 \times 4 \times 2$ supercell unit⁴⁷. We have further simulated various $2 \times 2 \times 2$ CO states from combinations of the unstable M and L phonon modes. The CO structures were relaxed with a 350 eV energy cutoff for the plane-wave basis and a $4 \times 4 \times 2$ grid sampling in the momentum space Brillouin zone. To elucidate the electronic properties of these COs, we performed electronic band structure unfolding and projections based on the Wannier models derived from DFT ground states, using Wannier 90 code.

Acknowledgements

This work was supported by the Air Force Office of Scientific Research Young Investigator Program under grant FA9550-19-1-0063, and by the STC Center for Integrated Quantum Materials (NSF grant no. DMR-1231319). The work is funded in part by the Gordon and Betty Moore Foundation's EPIQS Initiative, Grant GBMF9070 to JGC. The works at Max Planck POSTECH/Korea Research Initiative were supported by the National Research Foundation of Korea, Ministry of Science, Grant No. 2016K1A4A4A01922028 and 2020M3H4A2084417. B.R.O. and S.D.W. were supported by the National Science Foundation (NSF) through Enabling Quantum Leap: Convergent Accelerated Discovery Foundries for Quantum Materials Science, Engineering and Information (Q-AMASE-i): Quantum Foundry at UC Santa Barbara (DMR-1906325). This research used resources of the Advanced Light Source, a U.S. DOE Office of Science User Facility under contract no. DE-AC02-05CH11231. M.K. acknowledges a Samsung Scholarship from the Samsung Foundation of Culture. B.R.O. acknowledges support from the California NanoSystems Institute through the Elings Fellowship program.

References

1. Ortiz, B. R. *et al.* New kagome prototype materials: Discovery of KV₃Sb₅, RbV₃Sb₅, and CsV₃Sb₅. *Phys. Rev. Mater.* **3**, 94407 (2019).
2. Ortiz, B. R. *et al.* CsV₃Sb₅: a Z₂ topological kagome metal with a superconducting ground state. *Phys. Rev. Lett.* **125**, 247002 (2020).
3. Keimer, B., Kivelson, S. A., Norman, M. R., Uchida, S. & Zaanen, J. From quantum matter to high-temperature superconductivity in copper oxides. *Nature* **518**, 179–186 (2015).
4. Si, Q., Yu, R. & Abrahams, E. High-temperature superconductivity in iron pnictides and chalcogenides. *Nat. Rev. Mater.* **1**, 1 (2016).
5. Cao, Y. *et al.* Unconventional superconductivity in magic-angle graphene superlattices. *Nature* **556**, 43–50 (2018).
6. Jiang, Y.-X. *et al.* Unconventional chiral charge order in kagome superconductor KV₃Sb₅. *Nat. Mater.* **20**, 1353–1357 (2021).
7. Zhao, H. *et al.* Cascade of correlated electron states in a kagome superconductor CsV₃Sb₅. *Nature* **599**, 216–221 (2021).
8. Shumiya, N. *et al.* Intrinsic nature of chiral charge order in the kagome superconductor RbV₃Sb₅. *Phys. Rev. B* **104**, 035131 (2021).
9. Li, H. *et al.* Rotation symmetry breaking in the normal state of a kagome superconductor KV₃Sb₅. *Nat. Phys.* (2022) doi:10.1038/s41567-021-01479-7.
10. Xiang, Y. *et al.* Twofold symmetry of c-axis resistivity in topological kagome superconductor CsV₃Sb₅ with in-plane rotating magnetic field. *Nat. Commun.* **12**, 6727 (2021).
11. Yu, L. *et al.* Evidence of a hidden flux phase in the topological kagome metal CsV₃Sb₅. *arXiv* 2107.10714 (2021).
12. Ortiz, B. R. *et al.* Superconductivity in the Z₂ kagome metal KV₃Sb₅. *Phys. Rev. Mat.* **5**, 034801 (2021).
13. Yin, Q. *et al.* Superconductivity and normal-state properties of kagome metal RbV₃Sb₅ single crystals. *Chinese Phys. Lett.* **38**, 037403 (2021).
14. Wu, X. *et al.* Nature of Unconventional Pairing in the Kagome Superconductors A V₃Sb₅ (A = K, Rb, Cs). *Phys. Rev. Lett.* **127**, 177001 (2021).
15. Tazai, R., Yamakawa, Y., Onari, S. & Kontani, H. Mechanism of exotic density-wave and beyond-Migdal unconventional superconductivity in kagome metal AV₃Sb₅ (A=K, Rb, Cs). *Arxiv* 2107.05372 (2021).
16. Zhou, X. *et al.* Origin of charge density wave in the kagome metal CsV₃Sb₅ as revealed by optical spectroscopy. *Phys. Rev. B* **104**, L041101 (2021).
17. Li, H. *et al.* Observation of Unconventional Charge Density Wave without Acoustic Phonon Anomaly in Kagome Superconductors AV₃Sb₅ (A=Rb, Cs). *Phys. Rev. X* **11**, 031050 (2021).
18. Nakayama, K. *et al.* Multiple energy scales and anisotropic energy gap in the charge-density-wave phase of the kagome superconductor CsV₃Sb₅. *Phys. Rev. B* **104**, L161112 (2021).
19. Liu, Z. *et al.* Charge-Density-Wave-Induced Bands Renormalization and Energy Gaps in a Kagome Superconductor RbV₃Sb₅. *Phys. Rev. X* **11**, 41010 (2021).
20. Kang, M. *et al.* Twofold van Hove singularity and origin of charge order in topological kagome superconductor CsV₃Sb₅. *Nat. Phys.* (2022) doi:10.1038/s41567-021-01451-5.

21. Guo, H. M. & Franz, M. Topological insulator on the kagome lattice. *Phys. Rev. B* **80**, 113102 (2009).
22. Xu, G., Lian, B. & Zhang, S.-C. Intrinsic Quantum Anomalous Hall Effect in the Kagome Lattice Cs₂LiMn₃F₁₂. *Phys. Rev. Lett.* **115**, 186802 (2015).
23. Tang, E., Mei, J.-W. & Wen, X.-G. High-Temperature Fractional Quantum Hall States. *Phys. Rev. Lett.* **106**, 236802 (2011).
24. Yu, S. L. & Li, J. X. Chiral superconducting phase and chiral spin-density-wave phase in a Hubbard model on the kagome lattice. *Phys. Rev. B* **85**, 4–7 (2012).
25. Kiesel, M. L., Platt, C. & Thomale, R. Unconventional fermi surface instabilities in the kagome hubbard model. *Phys. Rev. Lett.* **110**, 126405 (2013).
26. Wang, W., Li, Z., Xiang, Y. & Wang, Q. Competing electronic orders on kagome lattices at van Hove filling. *Phys. Rev. B* **87**, 115135 (2013).
27. Tan, H., Liu, Y., Wang, Z. & Yan, B. Charge density waves and electronic properties of superconducting kagome metals. *Phys. Rev. Lett.* **127**, 046401 (2021).
28. Christensen, M. H., Birol, T., Andersen, B. M. & Fernandes, R. M. Theory of the charge density wave in AV₃Sb₅ kagome metals. *Phys. Rev. B* **104**, 214513 (2021).
29. Subedi, A. Hexagonal-to-base-centered-orthorhombic 4Q charge density wave order in kagome metals KV₃Sb₅, RbV₃Sb₅, and CsV₃Sb₅. *Phys. Rev. Mater.* **6**, 015001 (2022).
30. Liang, Z. *et al.* Three-Dimensional Charge Density Wave and Surface-Dependent Vortex-Core States in a Kagome Superconductor CsV₃Sb₅. *Phys. Rev. X* **11**, 31026 (2021).
31. Ortiz, B. R. *et al.* Fermi Surface Mapping and the Nature of Charge-Density-Wave Order in the Kagome Superconductor CsV₃Sb₅. *Phys. Rev. X* **11**, 41030 (2021).
32. Li, H. *et al.* Spatial symmetry constraint of charge-ordered kagome superconductor.
33. Ratcliff, N., Hallett, L., Ortiz, B. R., Wilson, S. D. & Harter, J. W. Coherent phonon spectroscopy and interlayer modulation of charge density wave order in the kagome metal CsV₃Sb₅. *Phys. Rev. Mater.* **5**, L111801 (2021).
34. Luo, J. *et al.* Star-of-David pattern charge density wave with additional modulation in the kagome superconductor CsV₃Sb₅ revealed by ⁵¹V-NMR and ^{121/123}Sb-NQR. *arXiv* 2108.10263 (2021).
35. Ye, Z., Luo, A., Yin, J.-X., Hasan, M. Z. & Xu, G. Structural instability and charge modulations in the Kagome superconductor CsV₃Sb₅. *arXiv* 2111.07314 (2021).
36. Hu, Y. *et al.* charge order assisted topological surface states and flat bands in the kagome superconductor CsV₃Sb₅. *Sci. Bull.* (2022).
37. Luo, H. *et al.* Electronic Nature of Charge Density Wave and Electron-Phonon Coupling in Kagome Superconductor KV₃Sb₅. *Nat. Commun.* **13**, 273 (2022).
38. Cho, S. *et al.* Emergence of new van Hove singularities in the charge density wave state of a topological kagome metal RbV₃Sb₅. *Phys. Rev. Lett.* **127**, 236401 (2021).
39. Hu, Y. Rich Nature of Van Hove Singularities in Kagome Superconductor CsV₃Sb₅ Yong. *arXiv* 2106.05922 (2021).
40. Rossnagel, K. On the origin of charge-density waves in select layered transition-metal dichalcogenides. *J. Phys. Condens. Matter* **23**, (2011).
41. Brouet, V. *et al.* Angle-resolved photoemission study of the evolution of band structure and charge density wave properties in RTe₃. *Phys. Rev. B* **77**, 235104 (2008).
42. Oey, Y. M. *et al.* Fermi level tuning and double-dome superconductivity in the kagome metals CsV₃Sb_{5-x}Sn_x. *arXiv* 2110.10912 (2021).
43. Kresse, G. & Furthmüller, J. Efficiency of ab-initio total energy calculations for metals

- and semiconductors using a plane-wave basis set. *Comput. Mater. Sci.* **6**, 15–50 (1996).
44. G. Kresse & Furthmüller, J. Efficient iterative schemes for ab initio total-energy calculations using a plane-wave basis set. *Phys. Rev. B* **54**, 11169–11186 (1996).
 45. Perdew, J. P., Burke, K. & Ernzerhof, M. Generalized gradient approximation made simple. *Phys. Rev. Lett.* **77**, 3865–3868 (1996).
 46. Blochl, P. E. Projector augmented-wave method. *Phys. Rev. B* **50**, 17953–17979 (1994).
 47. Togo, A. & Tanaka, I. First principles phonon calculations in materials science. *Scr. Mater.* **108**, 1–5 (2015).

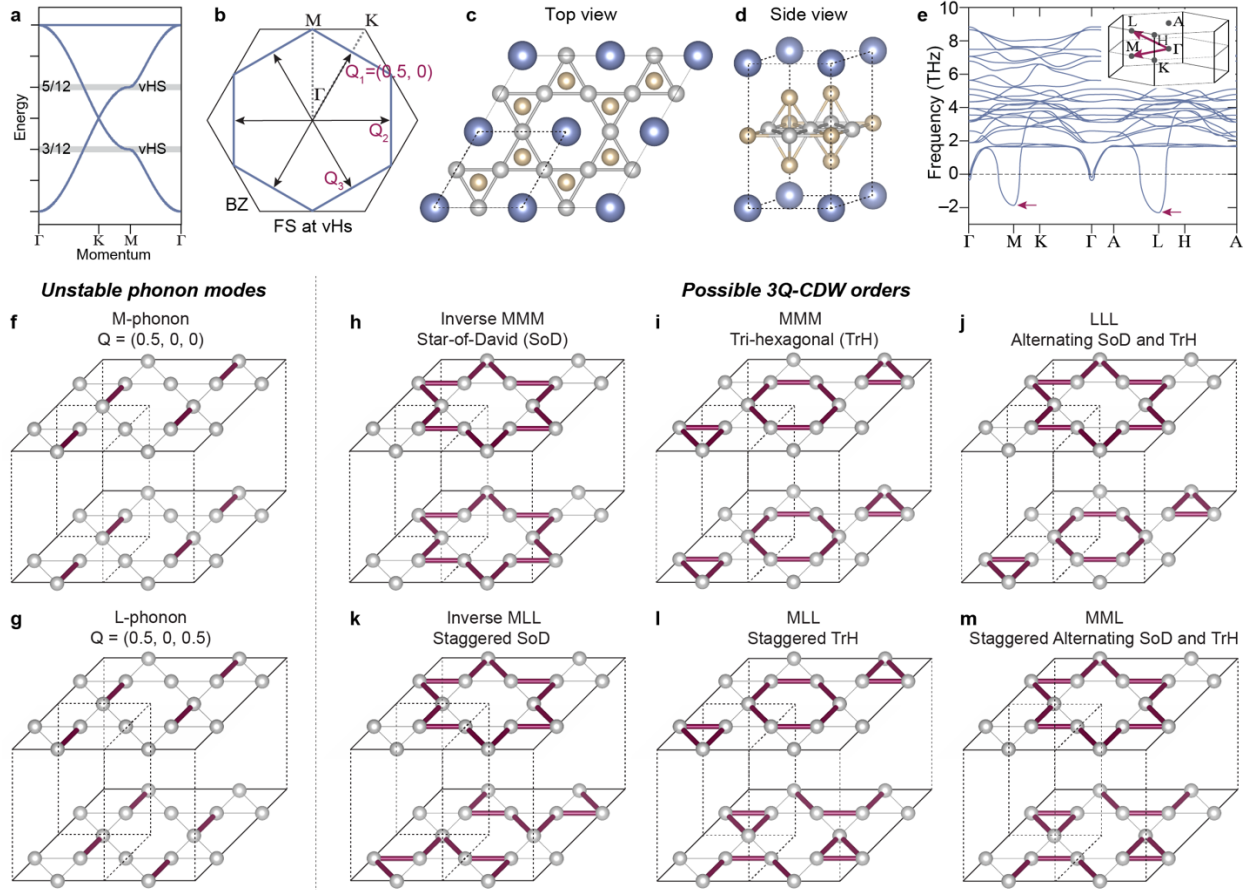


Figure 1 | Possible microscopic structures of the three-dimensional charge order (3D-CO) in kagome metal AV_3Sb_5 . **a**, Tight-binding electronic structure of an ideal kagome lattice. Grey-shaded lines mark the vHS filling fractions at 3/12 and 5/12. **b**, Perfectly nested hexagonal Fermi surface of the kagome lattice at the vHS filling fractions. Double-headed arrows indicate three symmetry-equivalent nesting vectors Q_1 , Q_2 , and Q_3 . **c,d**, Crystal structure of the AV_3Sb_5 with a V-kagome net. Dashed lines mark the unit cell in the undistorted phase. **e**, Calculated phonon dispersion of CsV_3Sb_5 showing instabilities of the pristine structure at M and L . Inset shows the Brillouin zone. **f,g**, Lattice distortions corresponding to the instabilities at M and L phonons, respectively. **h-m**, Possible structures of the 3D-CO in AV_3Sb_5 based on 3 Q -combinations of the M and L phonons.

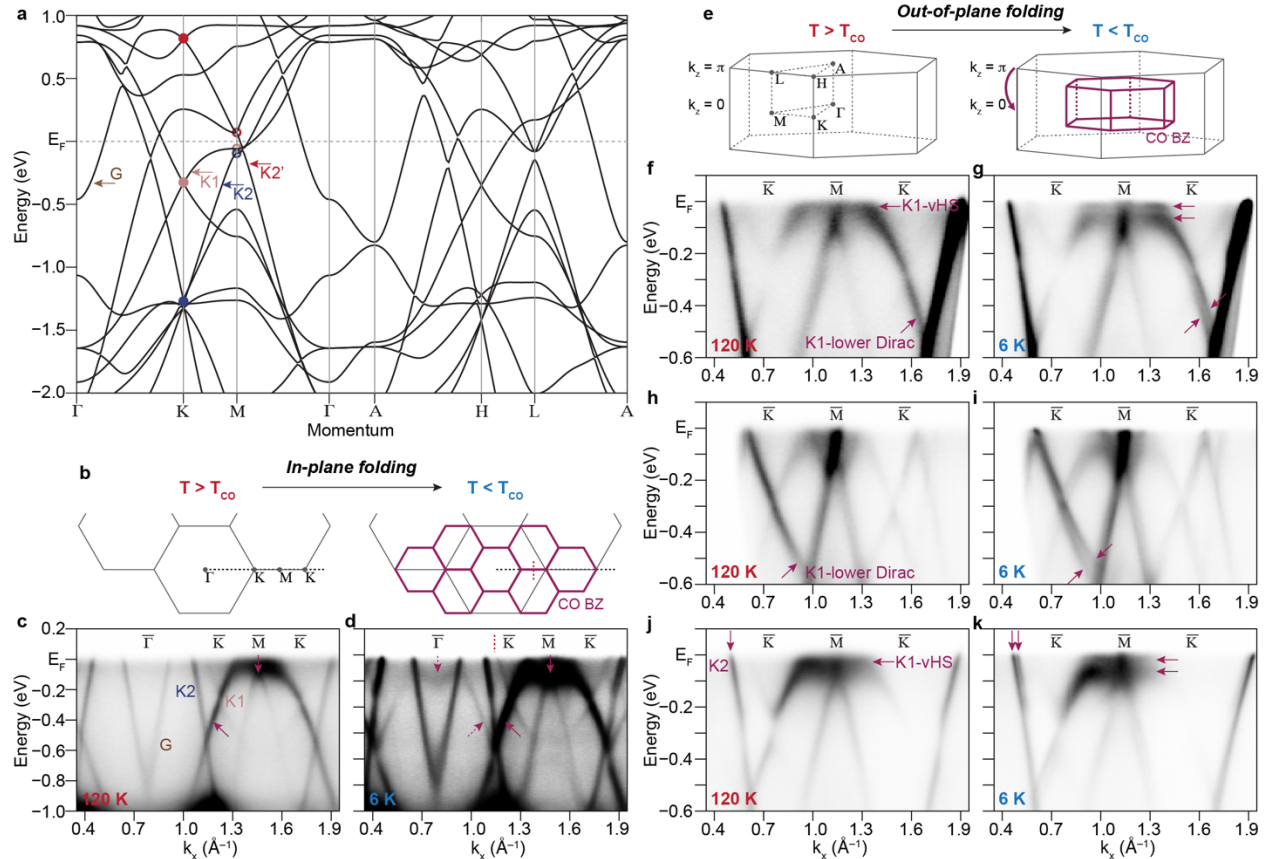


Figure 2 | Two distinct types of electronic reconstructions in CsV_3Sb_5 induced by 3D-CO. **a**, DFT band structure of CsV_3Sb_5 showing four bands crossing the Fermi level: G , $K1$, $K2$, and $K2'$ -bands. The Dirac points at K and vHS at M emerging from the $K1$, $K2$, and $K2'$ kagome bands are marked with filled and open circles, respectively. **b-d**, Electronic reconstruction from the in-plane component of charge order. **b**, Schematics of the in-plane folding of the Brillouin zone. **c,d**, Experimental band dispersion of CsV_3Sb_5 measured at 120 K and 6 K (above and below T_{CO}), respectively. Solid arrows in **c,d** mark the original bands, while the dashed arrows in **d** indicate the replica bands. **e-k**, Electronic reconstruction from the out-of-plane component of 3D-CO. **e**, Schematics of the out-of-plane folding of the Brillouin zone. Panels **f,h,j** (**g,i,k**) represent the dispersions measured above (below) T_{CO} , at the first Brillouin zone with photon energy 86 eV, at the second Brillouin zone with photon energy 86 eV, and at the first Brillouin zone with photon energy 113 eV, respectively. Solid arrows in **g,i,k** indicate the doubling or splitting of the kagome bands in the 3D-CO state.

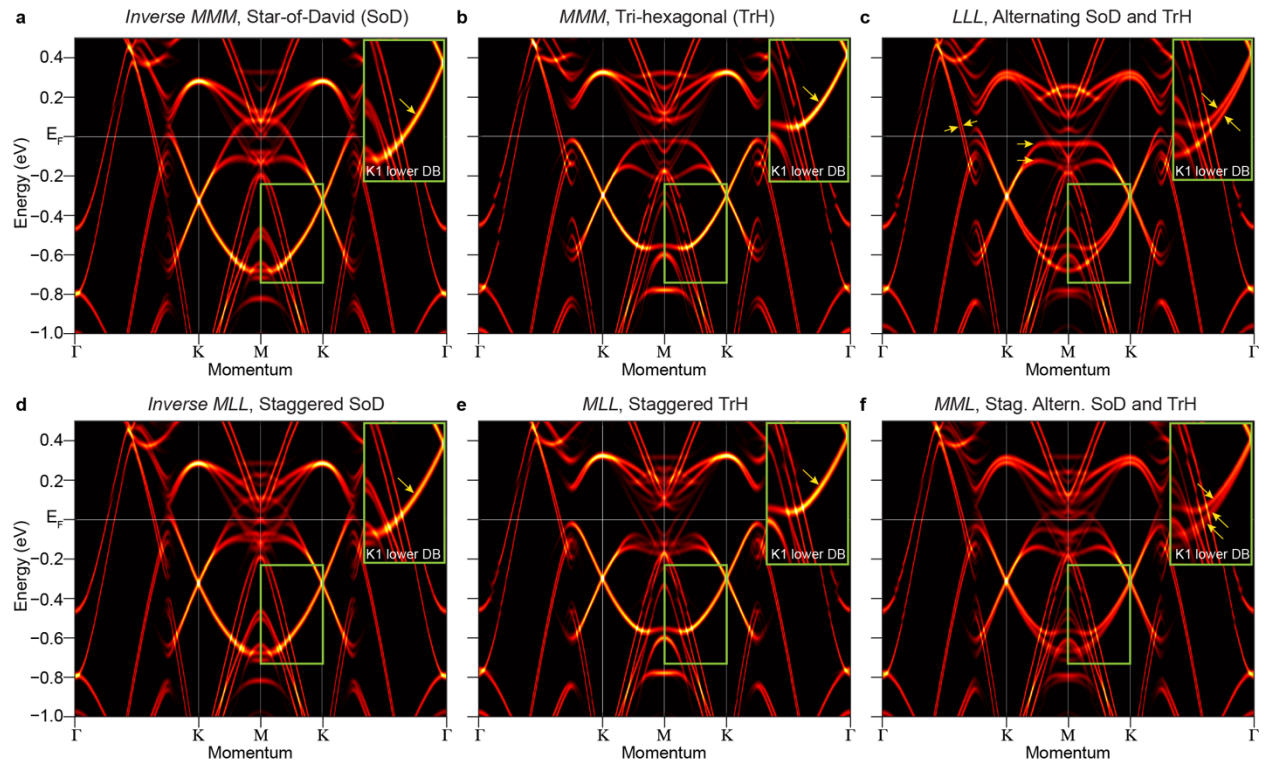


Figure 3 | Theoretical calculation of electronic reconstruction in AV_3Sb_5 and its dependence on the microscopic structure of 3D-CO. a-f, Calculated dispersion of CsV_3Sb_5 at $k_z = 0$ in the inverse *MMM*, *MMM*, *LLL*, inverse *MLL*, *MLL*, and *MML* phases, respectively. For simplicity, the dispersion is unfolded along the in-plane momentum direction. For the inverse *MLL*, *MLL* and *MML* phases (d-f) the calculation is averaged over three C_2 symmetric charge order domains to account for the macroscopic beam spot size. The insets zoom in the behavior of the lower K1 Dirac band, whose splitting sensitively depends on the microscopic structure of 3D-CO (see yellow arrows).

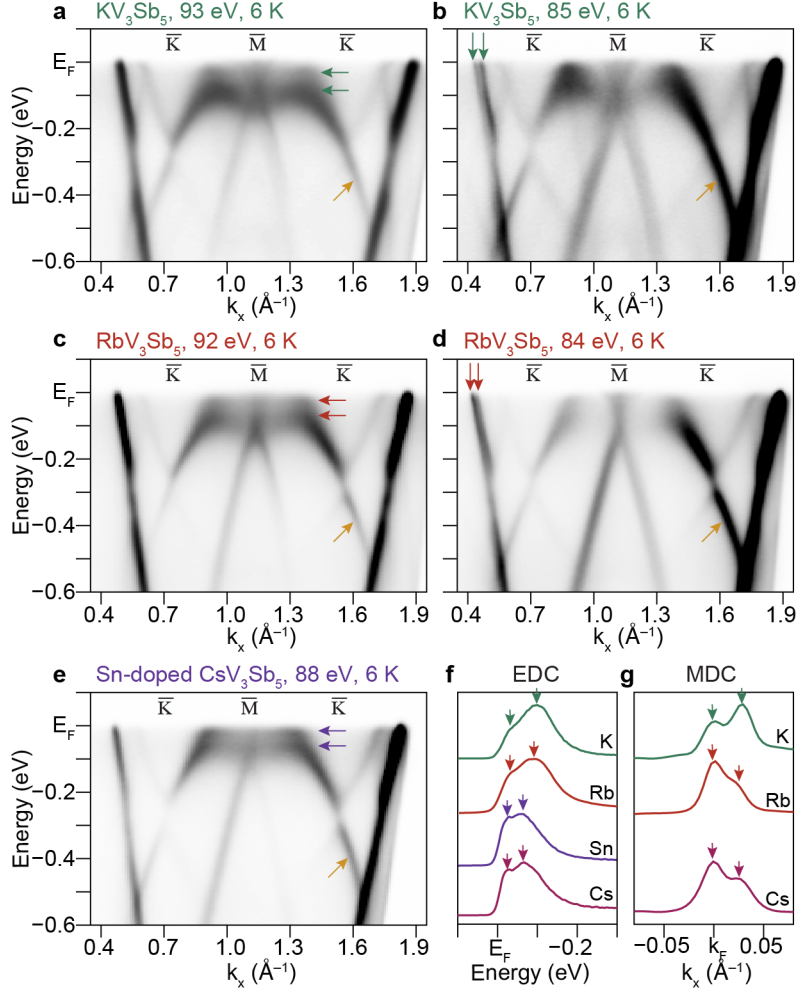


Figure 4 | Electronic reconstructions in KV₃Sb₅, RbV₃Sb₅, and Sn-doped CsV₃Sb₅ in 3D-CO state. **a-e**, ARPES spectra of KV₃Sb₅ (a,b) RbV₃Sb₅ (c,d), and Sn-doped CsV₃Sb₅ (e) measured at 6 K. The spectra in a-e are collected with 93 eV, 85 eV, 92 eV, 84 eV, and 88 eV photons, respectively. Green, red, and purple arrows indicate the splitting of K1-vHS and K2-band. Corresponding energy-distribution-curves (EDCs) and momentum-distribution curves (MDCs) are shown in f,g (see below). Yellow arrows highlight the absence of splitting on the lower Dirac band of K1, which is markedly different from the case of CsV₃Sb₅ in Fig. 2g,i. **f**, EDCs measured near the Fermi momentum (k_F) of the K1-band. Arrows highlight the splitting of K1-band near vHS. **g**, MDCs of the K2-band measured at the Fermi energy (E_F). Arrows highlight the splitting of the K2-band.